



Morphological effect of ceria-supported platinum catalyst on low-temperature ethylene oxidation

Haiying Wei^{a,b}, Tongtong Wei^{a,c}, Licheng Li^{a,c,*}, Tingwei Zhang^{a,*}, Farzad Seidi^a, Yongcan Jin^a, Huining Xiao^{b,**}

^a Jiangsu Co-Innovation Center of Efficient Processing and Utilization of Forest Resources, International Innovation Center for Forest Chemicals and Materials, Nanjing Forestry University, Nanjing 210037, China

^b Department of Chemical Engineering, University of New Brunswick, Fredericton, NB E3B 5A3 Canada

^c College of Chemical Engineering, Nanjing Forestry University, Nanjing 210037, China

ARTICLE INFO

Keywords:

CeO₂
Ethylene oxidation
Morphology
Platinum
Oxygen species

ABSTRACT

Three types of Pt/CeO₂ catalysts with different support morphologies (rod (CeO₂-R), cube (CeO₂-C), and octahedron (CeO₂-O)) were synthesized especially for catalytically oxidizing C₂H₄ at low temperatures. The as-prepared catalysts exhibited strong shape-dependent catalytic activity in the order of Pt/CeO₂-O > Pt/CeO₂-C > Pt/CeO₂-R. Such unique performance is mainly attributed to the different steps of C₂H₄ oxidation associated with the variation of oxygen species activated by Pt/CeO₂ catalysts. Among the three catalysts, Pt/CeO₂-O had the least issue with the accumulation of intermediate species and consequently performed the highest low-temperature C₂H₄ catalytic oxidation activity. Moreover, the negative impact of water condensation on the catalyst can be readily eliminated by refreshing the catalyst with N₂ purging. Overall, this work led to a novel catalytic system for efficient low-temperature ethylene oxidation and a better understanding of the catalytic mechanism, thus benefiting the preservation of fruits and vegetables as one of the applications.

1. Introduction

Ethylene, a plant hormone released by fruits and vegetables (F&V), often leads to over-ripening and even decay of F&V, causing up to 80 % of product losses [1]. Moreover, C₂H₄ is also one of the harmful volatile organic compounds (VOCs), potentially resulting in the photochemical pollution of the atmosphere and anesthetic illness. Various techniques for VOC removal have been developed, including physical adsorption, chemical decomposition, catalytic oxidation, and so on [2,3]. Among them, low-temperature catalytic oxidation of ethylene is a promising and environmentally friendly approach to oxidizing the C₂H₄ into harmless CO₂ and H₂O [4–6]. To date, only several precious metal catalysts (e.g., Pt, Au, Ag) have been reported to possess the low-temperature catalytic activity of ethylene oxidation [4,7,8]. Nevertheless, the high cost of precious metals limits its wide application, and the use of such metals in catalysts often accounts for most of the cost of the technology. Therefore, it is critical to develop a highly efficient catalyst for low-temperature ethylene oxidation for better performance

and cost-effectiveness.

The supported Pt catalyst can catalytically oxidize the ethylene at room temperature, which is consequently considered one of the most appropriate candidates for fresh-keeping fruits and vegetables [4–6,9,10]. Equally important as the exploration of novel active species and promoters, much research attention has been focused on the regulation of catalytic support. To date, various materials, including SiO₂, ZrO₂, carbon, and so on, have been used for the catalytic oxidation of ethylene at low temperature [11]. Accordingly, several strategies of catalytic support regulation, e.g., porous structure construction, hydrophobic surface modification, acid property adjustment, and so on, were developed to improve the catalytic performance of catalysts [5,9]. Despite the significant progress has been achieved in that the past decades, more effective strategies for improving the ethylene oxidation performance of catalysts at low temperatures remain in high demand.

As one of the supports, CeO₂ has been widely applied in catalytic oxidation of typical VOCs, including carbon monoxide, methane, formaldehyde, toluene, etc., due to its unique redox behavior and high

* Corresponding authors at: International Innovation Center for Forest Chemicals and Materials, Nanjing Forestry University, Nanjing 210037, China.

** Corresponding author.

E-mail addresses: lhc0024@yahoo.com (L. Li), ztwei@njfu.edu.cn (T. Zhang), hxiao@unb.ca (H. Xiao).

oxygen storage capacity [12]. Also, the CeO₂-supported catalyst has been demonstrated to possess the ability to catalytically oxidize ethylene at low temperatures [13]. However, the previous catalytic studies were mainly carried out on CeO₂ polyhedrons [14]. There is a growing research interest in the morphological regulation of CeO₂ owing to its dramatic impact on the catalytic performance of CeO₂-related catalysts. For instance, Li et al. firstly reported that the CeO₂ rods were more reactive for CO oxidation than CeO₂ irregular particles [15]. Based on this, Overbury et al. further found that the reducibility and mobility of lattice oxygen of the ceria nano-shapes were in line with where CO oxidation activity, i.e., rods > cubes > octahedral [16]. However, the shape-dependent catalytic performance of CeO₂ is different over various reactions. Torrente-Murciano et al.'s results showed that the order in total oxidation performance of polycyclic aromatic hydrocarbons of CeO₂ was rod < cube < particle [17]. Instead, the CeO₂ cubes had the best selective oxidation performance of ethanol [18]. After being loaded with metal, the CeO₂-supported catalyst still exhibited morphology-related catalytic performance dramatically. In the HCHO oxidation, the temperature for 90 % CO conversion is 22 °C for CeO₂ rod-supported Pt catalyst, 40 °C, and 50 °C for CeO₂ nanoparticles and cube counterparts, respectively [19]. Conversely, the CeO₂ cube-supported Pd catalyst could completely oxidize the HCHO at 30 °C, while only 60 % and 5 % of HCHO conversion for Pd/CeO₂ octahedron and Pd/CeO₂ rod [20]. In lean methane combustion, the octahedral CeO₂-supported Pd catalysts showed the most excellent catalytic performance [21]. Clearly, the catalytic behaviors of ceria-supported catalysts in terms of ceria morphology are case-specific.

To date, shape-dependent Pt/CeO₂ catalyst for low-temperature C₂H₄ oxidation has not been reported yet. In consideration of the morphological importance of CeO₂, we herein synthesized CeO₂ rod, CeO₂ cube, and CeO₂ octahedron as the supports for low-temperature C₂H₄ oxidation. The C₂H₄ oxidation performance of various-shaped CeO₂-supported Pt catalysts was evaluated under different reaction conditions. The structures and catalytic behaviors of as-prepared catalysts were comprehensively characterized in an attempt to clarify the morphology-performance relationship of CeO₂-supported catalysts as well as to better elucidate the catalytic mechanisms.

2. Experimental

2.1. Materials

Cerium nitrate hexahydrate (Ce(NO₃)₃·6H₂O, analytically pure grade, Sinopharm Chemical Regent., Ltd.), sodium hydroxide (NaOH, analytically pure grade, Sinopharm Chemical Regent., Ltd), ethanol (C₂H₅OH, analytically pure grade, Sinopharm Chemical Regent., Ltd), sodium phosphate tribasic dodecahydrate (Na₃PO₄·12H₂O, analytically pure grade, Sinopharm Chemical Regent., Ltd) and tetraammineplatinum nitrate (Pt(NH₃)₄(NO₃)₂, ≥ 50.0 % Pt basis, Aladdin Chemistry Co., Ltd) were used as received without further purification. N₂ (99.999 %), O₂ (99.999 %), and 10 % H₂/Ar were purchased from Nanjing Special Gas Co., Ltd and a 50 ppm C₂H₄/N₂ gas mixture was purchased from Shanghai Weichuang Standard Gas Analytical Technology Co., Ltd.

2.2. Preparation of CeO₂ supports and Pt/CeO₂ catalysts

The synthesis of CeO₂ with the morphologies of rod, cube, and octahedron was reported previously [22]. In brief, 4.34 g of Ce(NO₃)₃·6H₂O and 48 g of NaOH were dissolved in 200 mL of deionized water and hydrothermally treated at 100 °C for 24 h, forming the CeO₂ rod (CeO₂-R). Simultaneously, CeO₂ cube (CeO₂-C) was generated when the hydrothermal temperature of the above-mixed solution was set at 180 °C. The resulting samples were collected by centrifugation, followed by washing with distilled water and ethanol separately for three times, and dried at 60 °C in the oven for 12 h. Moreover, CeO₂ octahedron (CeO₂-O) was synthesized using Ce(NO₃)₃·6 H₂O and Na₃PO₄·12H₂O as

the precursors. 2.17 g of Ce(NO₃)₃·6H₂O and 0.019 g of Na₃PO₄·12H₂O were dissolved in 200 mL of deionized water and hydrothermally treated at 170 °C for 12 h. The powders were collected and purified by the above-mentioned procedures to obtain the CeO₂-O.

Loading of Pt species on CeO₂ was performed by an incipient-wetness impregnation method using Pt(NH₃)₄(NO₃)₂ as the precursor. The impregnated mixture was aged overnight and then dried in air at 60 °C for 8 h. Followed by calcination in air at 300 °C for 2 h with a heating rate of 2 °C·min⁻¹, the CeO₂-supported Pt catalyst was achieved. The amount of Pt loaded in catalysts was 0.79 ± 0.01 wt % according to ICP analyses. To test the catalytic activity of pristine CeO₂ for the C₂H₄ oxidation, CeO₂-R, CeO₂-C, and CeO₂-O were also calcined under the same conditions.

2.3. Characterization

The Morphological structure of samples was observed by both scanning electron microscopy (SEM, Regulus 8100, Hitachi) and high-resolution transmission electron microscopy (HRTEM, FEI Talos-F200S), respectively. The scanning transmission electron microscope (STEM) and energy-dispersive X-ray spectroscopy (EDX) were operated at an accelerating voltage of 200 kV. X-ray diffraction (XRD) patterns of samples were obtained by scanning with an Ultima IV diffractometer from 20° to 80° with a step size of 0.02° at a scanning rate of 10 ° min⁻¹ via a Ni-filtered Cu Kα radiation (λ = 1.542 Å). The crystallite sizes (D) were estimated by the Scherrer equation. The surface area (S_{BET}) and pore volume (V_p) of catalysts were determined by nitrogen adsorption-desorption at -196 °C using a Quadrasorb-Evo analyzer, and their pore size distributions were achieved from adsorption isotherms by the BJH method. Moreover, all samples were pretreated with the vacuum at 200 °C for 4 h. The amount of Pt of ceria-based Pt catalysts was determined by inductively coupled plasma mass spectrometry (Agilent ICPMS 7700). X-ray photoelectron spectroscopy (XPS, Nexsa, 156 Thermo Fisher) analysis was performed on a monochromatic Al Kα X-ray beam (1486.6 157 eV). The voltage and beam for the measurements were 12 kV and 6 mA, respectively. The vacuum in the test chamber during the collection of spectra was kept at 5 × 10⁻⁹ m bar. After removing the background, the spectra were fitted to Lorentzian and Gaussianlines to determine the parameters of the components or individual peaks. All the binding energies of elements were corrected to the C1s peak (284.6 eV). UV Raman spectra were obtained on HORIBA Scientific LabRAM HR with a CCD detector at ambient temperature and moisture-free conditions. The wavelength of excitation light was 325 nm and the signals were sampled in the range from 200 cm⁻¹ to 1400 cm⁻¹.

CO-pulse chemisorption was carried out on the AutoChem II 2920 to evaluate the diameter and dispersion state of Pt species in various catalysts. The sample was placed in a U-shaped quartz tube and pre-reduced at 300 °C for 2 h in a 10 % H₂/Ar gas mixture (30 mL·min⁻¹). Afterward, the temperature was cooled to 30 °C under Ar flow (30 mL·min⁻¹), 10 % CO/Ar pulse stream was periodically injected until the saturation adsorption on the catalyst was reached. The stoichiometric ratio of Pt and CO atom was set as 1:1. Then, the diameter (d_{pt}) and dispersion (D_{pt}) of Pt were evaluated in the following formula according to the consumption of CO:

$$d_{pt} = \frac{60X_{pt}}{\rho_{pt}S_{pt}}$$

$$D_{pt} = \frac{10S_{pt}M_{pt}}{X_{pt}\alpha_{pt}N_A} \times 100\%$$

where X_{pt} is the amount of Pt loaded (%), ρ_{pt} the density of Pt (21.45 g cm⁻³), S_{pt} the surface area of Pt relative to the sample obtained from CO pulse chemisorption (m² g⁻¹), M_{pt} the molar weight of Pt (195.08 g mol⁻¹), α_{pt} the cross-sectional area of Pt atoms (8.06 × 10⁻²⁰ m² atom⁻¹) and N_A the Avogadro constant.

H₂-temperature programmed reduction (H₂-TPR) of samples was carried out in a TP-5000 apparatus. 100 mg of the sample loaded in a U-shaped quartz tube was pretreated in N₂ gas with a flow rate of 30 mL·min⁻¹ at 350 °C for 30 min and then cooled down to room temperature. A 10 % H₂/N₂ gas mixture (30 mL·min⁻¹) was introduced into the quartz reactor, which was also used as a reference gas. The test temperature was increased from room temperature to 750 °C at a rate of 10 °C·min⁻¹. O₂-temperature programmed desorption (O₂-TPD) was also conducted on the TP-5000 apparatus. 100 mg of the sample loaded in a U-shaped quartz tube was reduced in 10 % H₂/Ar gas mixture (30 mL·min⁻¹) at 300 °C for 120 min and then cooled down to room temperature in He flow (30 mL·min⁻¹). Next, it was stabilized by 10 % O₂/He (30 mL·min⁻¹) for 60 min. Finally, the test temperature was increased from room temperature to 500 °C at a rate of 10 °C·min⁻¹ in a He flow (30 mL·min⁻¹).

In-situ diffuse reflectance Fourier transform infrared spectroscopy (DRIFTS) was performed on a Nicolet 6700 spectroscope (Thermo Electron) equipped with a diffuse reflectance accessory and an MCT detector within wavenumber range of 4000~1000 cm⁻¹. The testing of CO-DRIFTS proceeded as follows: the catalyst was placed into a copper crucible in an in-situ chamber and pretreated by N₂ at 105 °C for 0.5 h and cooled down to room temperature in pure He flow. CO was introduced into the chamber at 30 °C for 0.5 h, followed by purging pure He to remove excessive and weakly adsorbed CO. The stable spectral signal was recorded after 32 scans with a resolution of 4 cm⁻¹. Moreover, the experimental process of C₂H₄-DRIFTS was also performed in an in-situ chamber, which was shown as follows: the catalyst powders were firstly pretreated in a pure N₂ flow (30 mL·min⁻¹) at 105 °C for 10 min and subsequently cooled down to 30 °C. Secondly, a mixed gas of C₂H₄ + N₂ (~100 ppm C₂H₄) with a flow rate of 30 mL·min⁻¹ was injected into an in-situ chamber. After being kept for 1 h, the gas stream of the in-situ chamber was changed to pure N₂ (30 mL·min⁻¹) with purging for 0.5 h. Finally, the equal-flow pure O₂ instead of pure N₂ was introduced to observe the transformation of the intermediate. All the pretreated samples needed to experience three periods. The spectral signal was sampled at the given time.

2.4. Catalytic performance evaluation

The ethylene oxidation of various catalysts was performed in a quartz tube micro-reactor with an inner diameter of 6 mm under atmospheric pressure. 100 mg of powdery sample was placed in the micro-reactor and in-situ reduced in 10 % H₂/Ar with a flow rate of 30 mL·min⁻¹ at 300 °C for 2 h. Subsequently, the reaction gas of 50 ppm of C₂H₄ / 21 % O₂ / 79 % N₂ flowed through the catalyst bed at 40 mL·min⁻¹ at a space velocity of 24000 mL h⁻¹g⁻¹. The prolonged experiment for 100 mg of sample was carried out at 50 °C with a flow rate of 40 mL·min⁻¹. Moreover, the reaction conditions of simulated F&V preservation of three Pt/CeO₂ catalysts were set at the temperature of 25 °C, 90 % relative humidity (RH), 10 ppm of C₂H₄ concentration, and GHSV of 24,000 mL h⁻¹g⁻¹. RH was adjusted by bubbling the water with N₂ flow in the incubator. The C₂H₄ concentrations in gas flow were online analyzed by GC 1690 gas chromatograph equipped with flame ionization detector (FID). The C₂H₄ conversion ($X_{C_2H_4}$), values of turnover frequency (TOF (s⁻¹)), and activation energies (E_a) implemented from the C₂H₄ conversion below 10% were determined according to the following formula and Arrhenius plot:

$$X_{C_2H_4} = \frac{C_0 - C_t}{C_0} \times 100\%$$

$$TOF_{Pt} = X_{C_2H_4} F_{C_2H_4} \frac{M_{Pt}}{m_{cat} X_{Pt} D_{Pt}}$$

$$\ln k = -\frac{E_a}{RT} + \ln A$$

where C_0 and C_t are the C₂H₄ concentrations in the inlet and outlet gases, $F_{C_2H_4}$ is the ethylene flow velocity (mol s⁻¹), k represents for reaction rate constant (mol s⁻¹), R is the universal gas constant (kJ mol⁻¹ K⁻¹), and T is the temperature of reaction (K).

3. Results and discussion

3.1. Textural properties

SEM and HRTEM images of various Pt/CeO₂ catalysts are shown in Fig. 1. The morphologies of as-synthesized Pt/CeO₂-R, Pt/CeO₂-C, and Pt/CeO₂-O appear to be rod, cubic and octahedral, which are identical to those of their corresponding various CeO₂ supports (as seen in Fig. S1). Pt/CeO₂-R catalyst has an average diameter of 10 ± 2 nm, a wide length distribution between 70 and 160 nm (Fig. 1(a1)), and selectively exposing (110) and (100) crystal planes (Fig. 1(a2) and Fig. 1(a3)). The edge lengths of Pt/CeO₂-C are mostly between 20 and 100 nm (Fig. 1(b) and Fig. 1(b1)), which selectively expose (100) crystal planes (Fig. 1(b2) and Fig. 1(b3)). As for Pt/CeO₂-O, it has edge lengths between 160 and 170 nm (Fig. 1(c) and Fig. 1(c1)) and is enclosed by (111) crystal planes (Fig. 1(c3)). From Fig. 1(c2), the extensive distortions of the crystal planes highlighted by the white oval in the image can be observed, implying the presence of point defects on the surface of Pt/CeO₂-O catalyst, as by the previous report [23,24]. In contrast, no such significant deformation appears in HRTEM images of Pt/CeO₂-C and Pt/CeO₂-R.

XRD patterns of various Pt/CeO₂ catalysts are shown in Fig. S2. Each pattern exhibits well-resolved diffraction peaks at 28.6°, 33.1°, 47.5°, 56.3°, 59.1°, 69.4°, 76.7°, and 79.0°, which are ascribed to the (111), (200), (220), (311), (222), (400), (331) and (420) planes of cubic fluorite CeO₂ (PDF No. 34-0394), respectively. No shift in diffraction peaks of CeO₂ is observed in three XRD patterns compared with standard values, suggesting the perfect crystal structure of ceria in three catalysts [21]. This also means that the point defects observed by HRTEM analyses only exist on the surface of CeO₂ rather than in the bulk of CeO₂. Additionally, the characteristic diffraction peaks of the Pt or PtO_x phase (at approximately 40 °) do not appear in XRD patterns of three Pt/CeO₂ catalysts, demonstrating the excellent dispersion of Pt nanoparticles [25, 26].

The porous architectures of various-shaped CeO₂-supported Pt catalysts were achieved by analyses of N₂ adsorption-desorption isotherms and pore size distribution curves (as seen in Fig. S3 and Fig. S4). Pt/CeO₂-C and Pt/CeO₂-O show the type II isotherms, suggesting their non-porous features. By comparison, Pt/CeO₂-R catalyst has a mesoporous structure due to its type IV isotherm characteristic [27]. As shown in Table 1, the Pt/CeO₂-R owns the highest surface area (60.5 m²·g⁻¹) while Pt/CeO₂-C and Pt/CeO₂-O samples exhibit the similarly lower surface area (6.9 m²·g⁻¹ and 2.8 m²·g⁻¹).

From all the above HRTEM images of Pt/CeO₂ catalysts, the crystallites of Pt-related phases are not observed, which may be attributed to the small size of Pt nanoparticles or relatively low Pt loading amount [21,28]. Thus, the dispersion of Pt species in various Pt/CeO₂ catalysts was further characterized by STEM-EDX mapping, CO-pulse chemisorption, and CO-DRIFTS. Fig. 2 shows that all the bright spots ascribed to the Pt element are evenly distributed in the outline of the corresponding catalyst, indicating that Pt nanoparticles are well dispersed in three Pt/CeO₂ catalysts. Furthermore, the Pt particle sizes (d_{Pt}) and dispersion of Pt/CeO₂ catalysts can be obtained from CO-pulse chemisorption. As listed in Table 1, the d_{Pt} values of Pt/CeO₂-R, Pt/CeO₂-C, and Pt/CeO₂-O are 5.6 nm, 5.8 nm, and 5.7 nm, respectively, and the dispersions (D_{Pt}) of Pt/CeO₂-R, Pt/CeO₂-C and Pt/CeO₂-O are 30.9 %, 30.3 %, and 31.0 %, respectively. CO-DRIFTS display the structural information of Pt nanoparticles of various catalysts. As displayed in Fig. S5, three Pt/CeO₂ catalysts show two bands assigned to the CO linearly adsorbed in the Pt step (2065 cm⁻¹) and terrace sites

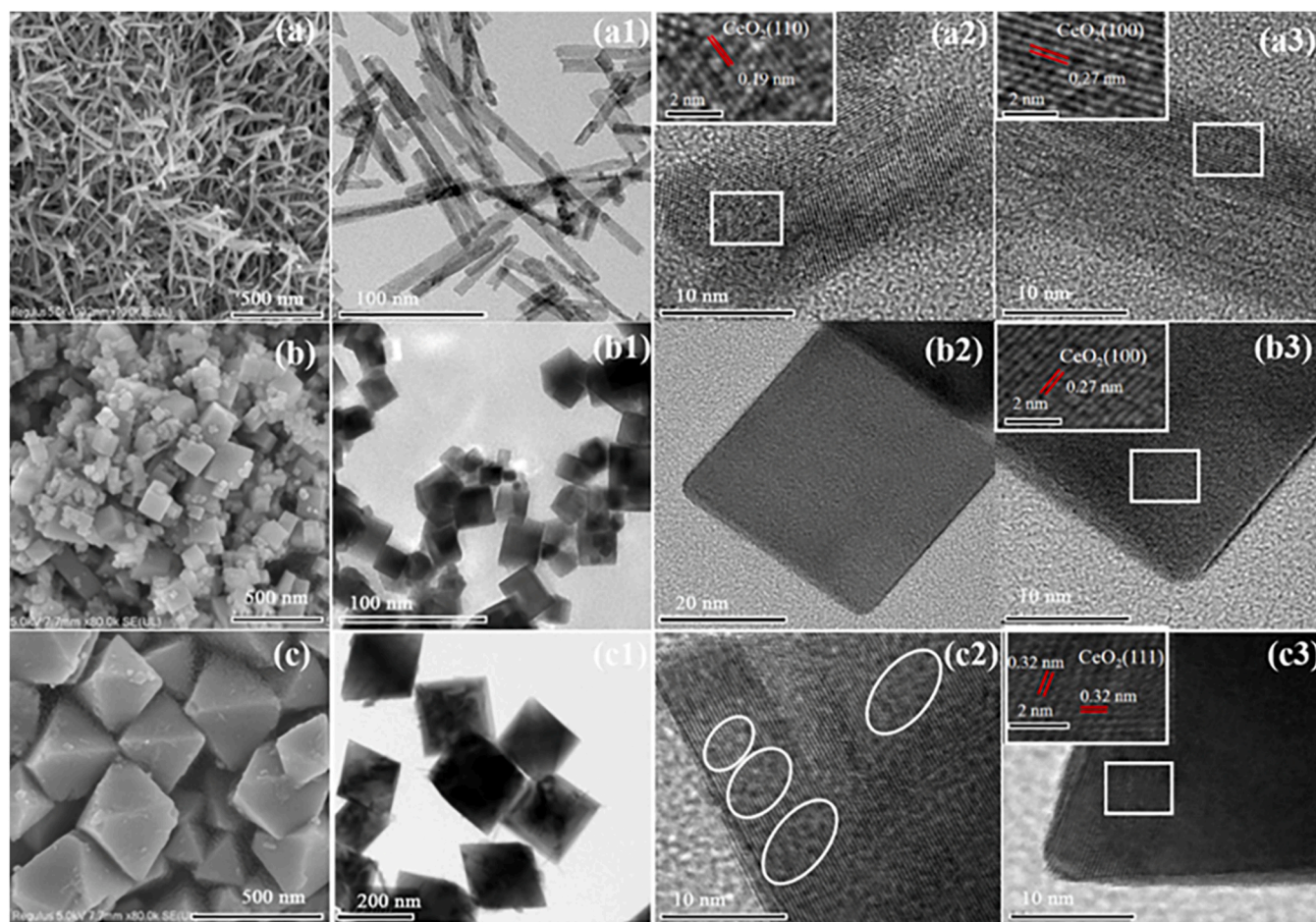


Fig. 1. SEM and HRTEM images of Pt/CeO₂-R (a, a1, a2 and a3), Pt/CeO₂-C (b, b1, b2 and b3) and Pt/CeO₂-O (c, c1, c2 and c3).

Table 1

Physiochemical properties of various morphological CeO₂-supported Pt catalyst.

Sample	Pt/CeO ₂ -R	Pt/CeO ₂ -C	Pt/CeO ₂ -O
S _{BET} (m ² g ⁻¹)	60.5	6.9	2.8
Mean Crystal size ^a (nm)	10	20	21
Pt loading ^b (wt%)	0.79	0.78	0.80
d _{Pt} ^c (nm)	5.6	5.8	5.7
D _{Pt} ^d (%)	30.9	30.3	31.0
X _i ^e (%)	21.3	20.8	21.2
Pt ⁰ /(Pt ⁰ +Pt ²⁺) (%)	67.8	70.8	77.5
Ce ³⁺ /(Ce ³⁺ +Ce ⁴⁺) (%)	27.2	28.4	30.4
O _{surf} /(O _{surf} +O _{latt}) (%)	33.8	35.4	38.1
I ₍₁₁₇₂₊₆₀₀₎ /I ₄₆₀ (%)	0.08	0.08	0.10

^a Estimated by the Scherrer equation, applied to the (111) reflection on fluorite CeO₂.

^b Determined by ICP-AAS.

^c Diameter of the loading Pt NPs measured by CO chemisorption, conducted at 30 °C.

^d Dispersion of the loading Pt NPs measured by CO chemisorption, conducted at 30 °C.

^e X_i is the fraction of total CO molecules bonded to stepped Pt sites, which could be calculated according to equation [30]. $X_i = \frac{I_{2065/3.7}}{I_{2065/3.7} + I_{2098}} \times 100\%$.

(2098 cm⁻¹), respectively [29]. The fraction of these two band intensities is usually utilized to reflect the morphology of Pt nanoparticles, which appears to be the almost same, thus demonstrating the similar Pt particle size for three catalysts, as consistent with the above analyses.

3.2. Catalytic evaluation

Three types of CeO₂ do not possess catalytic activity at low temperatures and all of them start to oxidize the ethylene at 145 °C or above (Fig. S6). After being loaded with Pt, the corresponding Pt/CeO₂ catalysts show significantly enhanced low-temperature C₂H₄ oxidation performance. As depicted in Fig. 3(a), the C₂H₄ oxidation performance of different Pt/CeO₂ catalysts strongly depends on the morphology of CeO₂. The C₂H₄ oxidation occurred at 20 °C for Pt/CeO₂-O, 30 °C for Pt/CeO₂-C, and 35 °C for Pt/CeO₂-R, respectively. With elevating reaction temperature, the increases in C₂H₄ conversion of various Pt/CeO₂ catalysts are dissimilar. The C₂H₄ conversion of Pt/CeO₂-O (50 °C) is the first to reach 100 % compared with those of Pt/CeO₂-C (70 °C) and Pt/CeO₂-R (80 °C), which indicates that the order in C₂H₄ catalytic oxidation performance follows: Pt/CeO₂-O > Pt/CeO₂-C > Pt/CeO₂-R.

Furthermore, the ethylene conversion as a function of the reaction temperature of three Pt/CeO₂ catalysts was repeatedly tested with three successive cycles. As also shown in Fig. 3(a), no obvious ethylene conversion changes were detected by measuring the reactivity by going downing and then going up the temperature. A smooth S-curve shape plot was obtained with three successive cycles, and the results indicated that all the Pt/CeO₂ catalysts possess favorable thermal catalytic stabilities.

Fig. 3(b) presents the results related to the long-term C₂H₄ conversion of three types of Pt/CeO₂ catalysts. No obvious decrease in C₂H₄ conversion was observed at above 50 h regardless of the type of catalyst. In addition, over the entire reaction process, no carbon-containing species other than CO₂ were presented in the final product according to the material balance obtained from the combined analyses of GC and

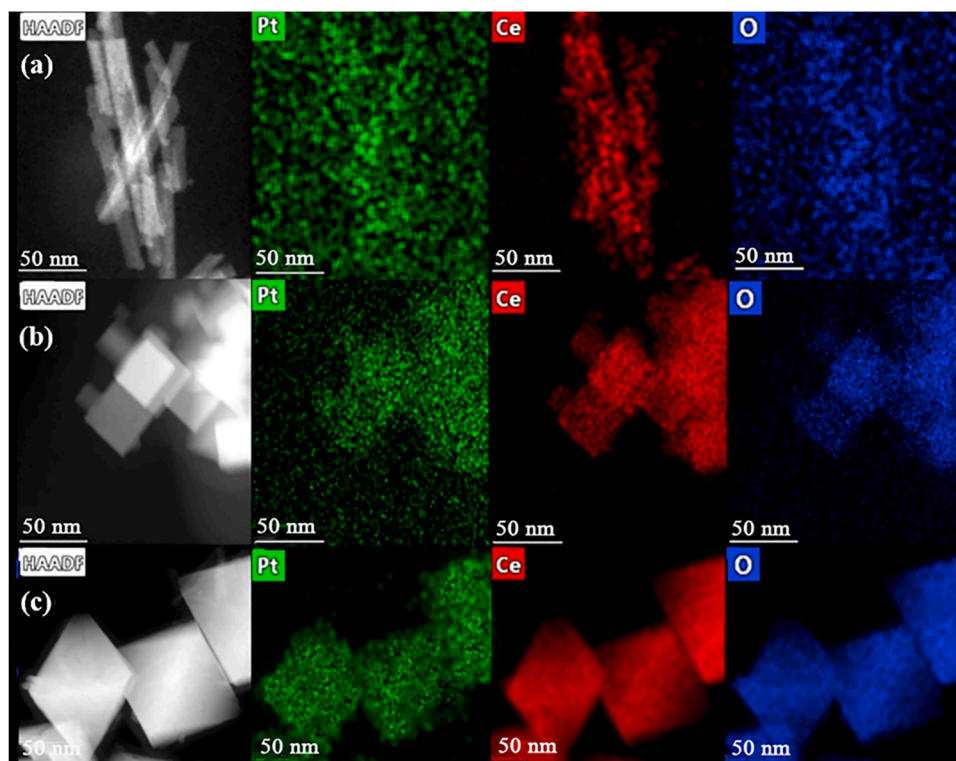


Fig. 2. Representative STEM-high-angle annular dark-field images and EDX mapping of Pt/CeO₂-R (a), Pt/CeO₂-C (b), and Pt/CeO₂-O (c).

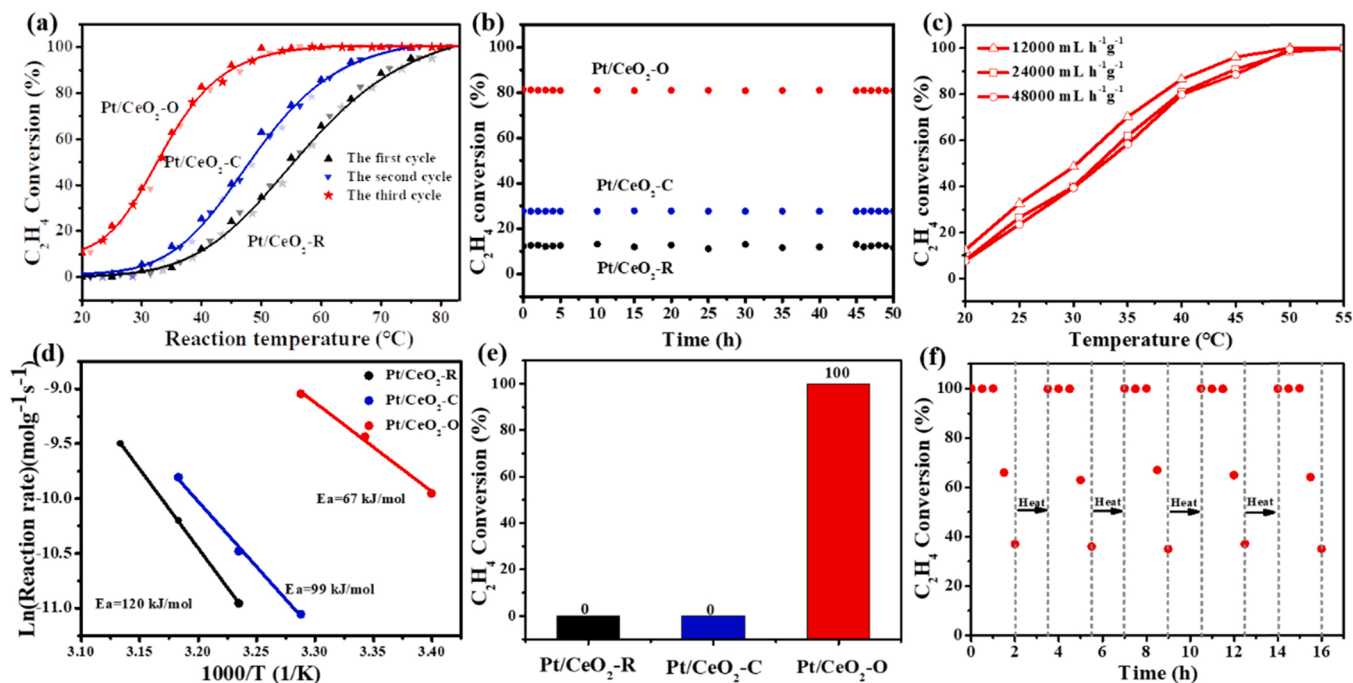


Fig. 3. C₂H₄ conversion as a function of reaction temperature of various morphological CeO₂-supported Pt catalysts (C₂H₄ 50 ppm, catalyst 0.1 g, GHSV 24000 mL h⁻¹ g⁻¹) (a), long-term experimental result (C₂H₄ 50 ppm, catalyst 0.1 g, 40 °C, GHSV 24000 mL h⁻¹ g⁻¹) (b), C₂H₄ conversion of Pt/CeO₂-O at various GHSV (C₂H₄ 50 ppm, catalyst 0.1 g) (c), Arrhenius plots of various Pt/CeO₂ catalysts (C₂H₄ 50 ppm, catalyst 0.02 g, GHSV 24000 mL h⁻¹ g⁻¹, C₂H₄ conversion < 10 %) (d), C₂H₄ conversion of various Pt/CeO₂ catalysts (C₂H₄ 10 ppm, catalyst 0.1 g, GHSV 24000 mL h⁻¹ g⁻¹, 25 °C, 90 % RH) (e), and ethylene durability of Pt/CeO₂-O catalyst (C₂H₄ 10 ppm, catalyst 0.1 g, GHSV 24000 mL h⁻¹ g⁻¹, 25 °C, 90 % RH) (f).

CO₂ detector (as described in SI), suggesting the complete oxidation of C₂H₄. The same conclusion was also reported extensively in literatures [4,8,10]. These results further demonstrate the excellent stability in C₂H₄ oxidation of Pt/CeO₂-O catalyst.

Fig. 3(c) displays the C₂H₄ conversion of Pt/CeO₂-O catalyst at different gas hourly space velocities (GHSV). It can be seen that GHSV has a slight effect on the catalytic performance of Pt/CeO₂-O catalyst, indicating the robust catalytic activities of Pt/CeO₂-O for the oxidation

of ethylene. Arrhenius plots, as shown in Fig. 3(d), provide the apparent activation energies (E_a) for C_2H_4 oxidation induced by various Pt/CeO₂ catalysts. The E_a values of Pt/CeO₂-O, Pt/CeO₂-C, and Pt/CeO₂-R are 67 kJ·mol⁻¹, 99 kJ·mol⁻¹, and 120 kJ·mol⁻¹, respectively. The lowest E_a value for Pt/CeO₂-O implies the easiest C_2H_4 conversion, which could be responsible for the highest ethylene oxidation activity of Pt/CeO₂-O. Furthermore, the distinctly different E_a values among three Pt/CeO₂ catalysts demonstrate their dissimilar low-temperature C_2H_4 oxidation mechanisms.

Based on these results, we further evaluated the catalytic performance of Pt/CeO₂-O, Pt/CeO₂-C, and Pt/CeO₂-R under the simulated reaction conditions for F&V preservation. As shown in Fig. 3(e), Pt/CeO₂-O enables the complete conversion of C_2H_4 at 25 °C (around ambient temperature) and 90 % of relative humidity (RH), while both Pt/CeO₂-C and Pt/CeO₂-R almost do not catalytically decompose any ethylene. Fig. 3(f) shows the ethylene conversion results of Pt/CeO₂-O over the range of 0–16 h under simulated F&V preservation condition. At the initial stage, Pt/CeO₂-O catalyst exhibits 100 % of ethylene conversion. With the extension of exposure time, the ethylene conversion was gradually decreased and only reached 38 % after 2 h. This decline in ethylene conversion of Pt/CeO₂-O catalyst could be attributed to the presence of moisture along with the water produced by the ethylene oxidation reaction. Fukuoka et al. [4] and Hao et al. [31] confirmed that water condensation could lead to the partial blockage of the active sites with ethylene molecules. The activity of such deactivated catalyst could be restored by heating treatment. As expected, Pt/CeO₂-O purged with N₂ at 150 °C for 60 min achieves the complete conversion of ethylene at 25 °C. The catalyst can maintain an equal catalytic performance even after 5 cycles implying the great potential of recyclable Pt/CeO₂-O in preventing F&V from over-ripening in practical applications.

3.3. Redox property and chemical state

As typical reducible support, the CeO₂ surface has the characteristics of the redox cycle of Ce³⁺/Ce⁴⁺, which is crucial to the catalytic performance of CeO₂-containing catalysts in most oxidation reactions, including low-temperature C_2H_4 oxidation [15,17,25]. The previous researches have demonstrated that the exposure of different crystal planes of CeO₂ predominantly influences the redox cycle of Ce³⁺/Ce⁴⁺ [15,27,32,33]. Above HRTEM analyses show that Pt/CeO₂-R selectively exposes (110) and (100) crystal planes of CeO₂, Pt/CeO₂-C selectively exposes (100) crystal planes of CeO₂ while Pt/CeO₂-O mainly encloses

(111) crystal planes of CeO₂. To verify this, the redox properties of different shaped CeO₂ and the chemical state of corresponding Pt catalysts were investigated thoroughly.

Ce3d spectra of various morphological CeO₂-supported Pt catalysts are shown in Fig. 4(a). Ten peaks resulting from the pairs of spin-orbit doublets can be identified through the deconvolution method, of which four peaks at 880.6, 885.1, 898.9, and 903.2 eV are contributed from the XPS signal of Ce³⁺ while the other six peaks at 882.1, 888.5, 898.1, 900.6, 906.9 and 916.6 eV arise from Ce⁴⁺ [34]. The observation of Ce³⁺ indicates the presence of a redox cycle of Ce³⁺/Ce⁴⁺ in three Pt/CeO₂ catalysts. As listed in Table 1, the content of Ce³⁺ in Pt/CeO₂-R, Pt/CeO₂-C, and Pt/CeO₂-O are 27.2 %, 28.4 %, and 30.4 %, respectively, which was calculated by $S1/(S1 + S2)$ in terms of the peak area of Ce³⁺ (S1) and Ce⁴⁺ (S2). The higher content of Ce³⁺ indicates the existence of more redox cycle of Ce³⁺/Ce⁴⁺, which also means the existence of more oxygen vacancies in the catalyst [23]. The same demonstration could also be achieved by UV Raman spectra. As shown in Fig. 5, the intense band of three catalysts at 460 cm⁻¹ is ascribed to the F2g vibrational mode of the CeO₂ fluorite-type structure, and two broad bands centered at ca. 600 and 1172 cm⁻¹ are attributed to defect-induced (D) mode and second-order longitudinal optical (2LO) mode brought by the presence of Ce³⁺ [25,27]. The ratio of $I_{(1172+600)}/I_{460}$ displayed in Table 1

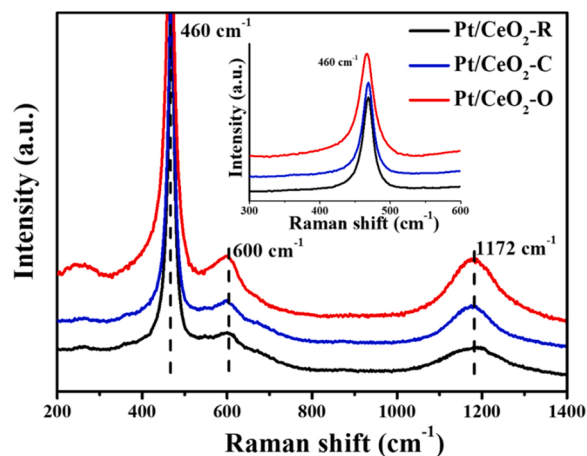


Fig. 5. UV Raman spectra of various Pt/CeO₂ catalysts. Inset is the full version of Raman band at 460 cm⁻¹.

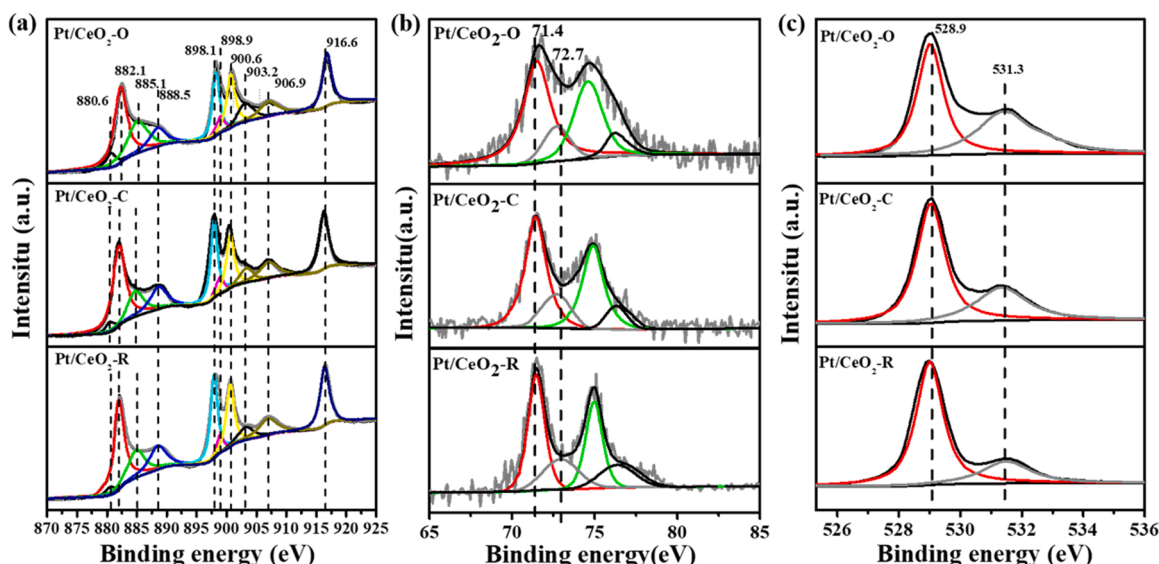


Fig. 4. XPS spectra of Ce3d (a), Pt4f (b) and O1s (c) of various Pt/CeO₂ catalysts.

represents the concentration of oxygen vacancy in three Pt/CeO₂ catalysts, the order in those values matches up with that of the above Ce3d XPS analyses.

The redox properties of various morphological CeO₂ and corresponding supported Pt catalysts were further studied with H₂-TPR. As depicted in Fig. 6(a), all the H₂-TPR patterns can be divided into three temperature zones of room temperature ~ 300 °C, 300 ~ 600 °C, and 600 ~ 1000 °C, which are assigned to the reduction of the surface lattice oxygen in the vicinity of Pt (i.e. Pt-O-Ce), surface/subsurface lattice oxygen and bulk-phase lattice oxygen of CeO₂, respectively [25,35]. Different reduction temperatures of three Pt/CeO₂ catalysts indicate that the different exposed facets of CeO₂ due to various shapes indeed have dissimilar redox properties [22,25,27]. The reduction temperatures associated with surface/subsurface lattice oxygen of CeO₂ of three Pt/CeO₂ catalysts are decreased to some extent compared with those of corresponding CeO₂ (317.0 ~ 435.4 °C versus 462.2 ~ 518.3 °C). This could be attributed to the formation of the Pt-O-Ce bond in Pt/CeO₂ catalysts due to the Pt incorporation [36]. Note that the temperature order in the CeO₂ reduction of catalysts is exactly opposite to that of supports. The CeO₂-O with the highest reduction temperature of CeO₂ (518.3 °C) in turn shows the easiest reduction property (317.0 °C) after being loaded with Pt species. By comparison, Pt incorporation only decreases dozens of degrees centigrade in reduction temperature of CeO₂ for rod-morphological CeO₂. This indicates Pt species have an obviously stronger interaction with (111) crystal plane of CeO₂ than that with other ones of CeO₂, as reported previously [37]. Apparently, the Pt/CeO₂ interactions in different morphological Pt/CeO₂ catalysts are sensitive to the exposed crystal planes of CeO₂.

Pt 4f XPS spectra were obtained to reveal the Pt chemical state of Pt/CeO₂-R, Pt/CeO₂-C and Pt/CeO₂-O catalysts. As shown in Fig. 4(b), the peaks at 71.4 and 72.7 eV are ascribed to the XPS signal of metallic Pt⁰ and Pt²⁺, respectively [34]. As listed in Table 1, the contents of Pt⁰, calculated by S₁/(S₁ + S₂) according to the peak area of Pt⁰ (S₁) and the peak area of Pt²⁺ (S₂) in Pt/CeO₂-O, Pt/CeO₂-C, and Pt/CeO₂-R are 77.5 %, 70.8 %, and 67.8 %, respectively. Pt species are more liable to form the metallic Pt on octahedral CeO₂ compared with cube and rod ones. The oxygen molecules adsorbed on metallic Pt can be readily transferred to the Pt-CeO₂ interface for activation [38]. Therefore, the higher content of metallic Pt is beneficial to oxygen activation.

To further investigate the state of oxygen vacancies of all catalysts, the O₂-TPD characterization was conducted, and the results are shown in Fig. 6(b). The peak at low temperature (< 350 °C) can be identified by O₂, and the peaks at 350 ~ 700 °C can be aroused by O₂⁻ or O⁻ [21]. For three types of supports, the O₂-TPD pattern of CeO₂-R shows two peaks at 212 and 340 °C, CeO₂-C at 236 and 361 °C, and CeO₂-O at 281 and 397 °C. When Pt is loaded on CeO₂ with different morphologies, Pt/CeO₂-R shows two obvious peaks at 139 and 271 °C, Pt/CeO₂-C at 128 and 231 °C while Pt/CeO₂-O shows two significant peaks at 116 and

215 °C. From the results above, it can be seen that the areas of the peaks increase at low temperatures, while the temperatures corresponding to these peaks are lowered after Pt was deposited on different morphological supports. This phenomenon indicates that Pt species are in favor of O₂ produced. Compared to Pt/CeO₂-R and Pt/CeO₂-C, Pt/CeO₂-O exhibits the largest area and the lowest temperature of the peaks, suggesting that the most amount of activated oxygen species are formed on Pt/CeO₂-O surface.

The similar results can also be obtained by analysis of O1 s XPS spectra. As shown in Fig. 4(c), the asymmetric peaks of O1 s can be fitted as O_{latt} (528.9 eV) and O_{surf} (531.3 eV), which are assigned to the lattice oxygen (O²⁻) and surface adsorbed oxygen (O₂⁻, O⁻, O₂²⁻), respectively [25,34]. The latter ones are the oxygen species that participated in oxidation reactions. As listed in Table 1, the O_{surf} content calculated by S₁/(S₁ + S₂) in terms of the peak area of O_{surf} (S₁) and the peak area of O_{latt} (S₂) is 33.8 %, 35.4 %, and 38.1 % for Pt/CeO₂-R, Pt/CeO₂-C, and Pt/CeO₂-O, respectively. Obviously, this result is consistent with the findings from O₂-TPD analyses. Moreover, the aforementioned TPR results also show that Pt/CeO₂-O (127.5 °C) has the relatively lower reduction temperature than those of Pt/CeO₂-C (169.2 °C) and Pt/CeO₂-R (275.8 °C).

The state of oxygen species in the Pt-CeO₂ interface can be analyzed by reducing temperature of the Pt-O-Ce bond [36]. This demonstrates that oxygen species in Pt-CeO₂ interface of Pt/CeO₂-O are the most reactive, followed by those in Pt/CeO₂-C, and the least for those in Pt/CeO₂-R, which is also reflected by the order in desorption temperature of oxygen species from O₂-TPD analyses.

From the results above, it can be seen that the various morphological Pt/CeO₂ catalysts with dissimilar exposed crystal planes exhibit the noticeable difference in relation to redox properties and chemical states. Pt/CeO₂-O with exposure of (111) crystal planes of CeO₂ has the more redox cycle of Ce³⁺/Ce⁴⁺ and more oxygen vacancies than Pt/CeO₂-R with (110) and (100) crystal planes and Pt/CeO₂-C with (100) crystal planes of CeO₂. Moreover, Pt/CeO₂-O possesses the highest content of metallic Pt and the lowest interaction between Pt and CeO₂, which are considered to significantly improve the activation of adsorbed oxygen species of catalysts [39]. Accordingly, the states of oxygen species activated by various morphological Pt/CeO₂ catalysts are different and the orders in amount and reactivity are ranked as Pt/CeO₂-O > Pt/CeO₂-C > Pt/CeO₂-R.

3.4. C₂H₄ oxidation pathway

The mechanism for ethylene catalytic oxidation has been documented [4,6,9,10]. The oxidation of C₂H₄ into CO₂ and H₂O usually occurs through several reaction steps. One of the typical and well-received reaction pathways is described as follows: C₂H₄ and O₂ adsorb on the Pt site, and subsequently react to form adsorbed HCHO.

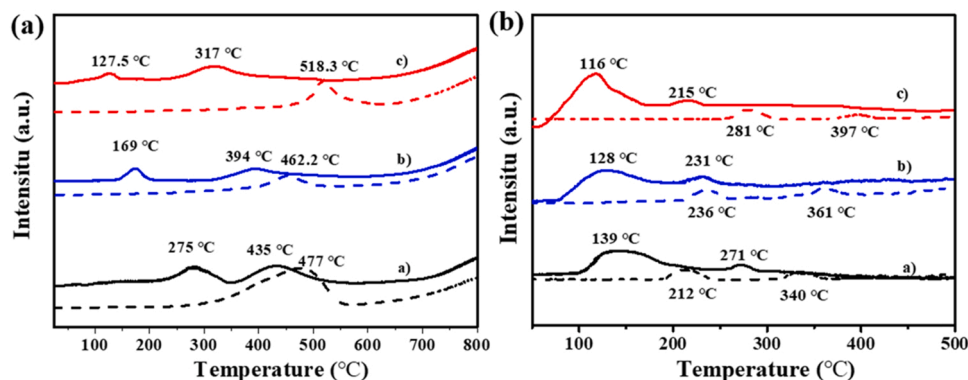


Fig. 6. (a) H₂-TPR patterns of various Pt/CeO₂ catalysts (solid line) and their corresponding CeO₂ (dotted line): a) Pt/CeO₂-R, b) Pt/CeO₂-C, c) Pt/CeO₂-O and (b) O₂-TPD patterns of various Pt/CeO₂ catalysts (solid line) and their corresponding CeO₂ (dotted line): a) Pt/CeO₂-R, b) Pt/CeO₂-C, c) Pt/CeO₂-O.

The as-formed HCHO is decomposed into atomic hydrogen (H) and CO species, which react with oxygen species to be converted to H₂O and CO₂, respectively. Meanwhile, a certain amount of HCOOH is generated from HCHO as the by-product on active sites and overflows to support. As mentioned above, C₂H₄ could be completely oxidized into CO₂ and H₂O by the catalysis of various Pt/CeO₂ catalysts. However, among these reaction steps, it remains unknown which step of C₂H₄ oxidation over Pt/CeO₂ catalysts is influenced profoundly by the morphological effect of CeO₂. This instead is crucial for understanding the structure-performance relationship of catalysts. Thus, the reaction pathway of C₂H₄ oxidation over various morphological CeO₂-supported Pt catalysts was studied by in-situ C₂H₄-DRIFTS.

Fig. 7 displays the representative DRIFTS spectra of various Pt/CeO₂ catalysts exposed successively in the atmosphere of C₂H₄ + N₂, pure N₂, and pure O₂, and all of them can be seen in Fig. S7 ~ Fig. S12 of the supporting material. Initially, in an atmosphere of C₂H₄ + N₂ with the continuous flowing of 60 min, three catalysts show dramatically different DRIFT spectra from each other. Pt/CeO₂-C shows two obvious bands at 1265 cm⁻¹ and 1487 cm⁻¹, ascribed to the γ (CH₂) and δ_{as} (CH₂) of adsorbed HCHO [40]. Compared with those of Pt/CeO₂-C, the intensities of these two bands of Pt/CeO₂-R are relatively weaker. This demonstrates the oxidation of ethylene over Pt/CeO₂-R and Pt/CeO₂-C proceeds through the intermediate species HCHO. In contrast, the HCHO signal is absent in the DRIFT spectra of Pt/CeO₂-O. Among the three catalysts, only the Pt/CeO₂-C shows an obvious band at 1403 cm⁻¹ ascribed to the out-of-plane bending vibration of methyl [41]. It was found that the C₂H₄ molecule adsorbed on metallic Pt and would form an ethylidyne before carbon-carbon bond breakage [42]. Thus, ethylene molecules may not dissociate rapidly after being adsorbed on Pt/CeO₂-C. Moreover, three catalysts all display the bands at 1360 cm⁻¹, 1538 cm⁻¹, and 2073 cm⁻¹, which are assigned to the ν_s (OCO), ν_a (OCO) of formate, and ν (CO) of linear-adsorbed CO, respectively [40,43]. As mentioned above, CO is the downstream reaction product of adsorbed HCHO, which demonstrates that Pt/CeO₂-R, Pt/CeO₂-C, and Pt/CeO₂-O can oxidize ethylene into CO. As the

by-product of adsorbed HCHO oxidation, formate is generated on three catalysts, but their signal intensities of formate (1360 and 1538 cm⁻¹) are varying, suggesting the different amounts of formate in three catalysts. The presence of formate signal in the DRIFT spectra of Pt/CeO₂-O reflects both rapid dissociation of C₂H₄ and fast oxidation of adsorbed HCHO on Pt/CeO₂-O.

At the second stage of N₂ purging, the band of Pt/CeO₂-R and Pt/CeO₂-O at around 2073 cm⁻¹ completely disappear while that of Pt/CeO₂-C declines in intensity. The absence of CO band in spectra of Pt/CeO₂-R and Pt/CeO₂-O is not explained by CO desorption because the weak-adsorbed CO appears at above 2150 cm⁻¹ [44]. Also, we did not collect the information on CO in the off-gas of three catalysts during our catalytic evaluation process. Hence, the decrease in CO signal intensity of band could be attributed to the oxidation of linear-adsorbed CO by lattice oxygen of catalysts at this stage of oxygen-free environment. Moreover, other intermediate species, e.g., formate, ethylidyne etc., of three catalysts do not show the observably decrease in signal intensity with N₂ purging.

At the third stage, admission of oxygen into chamber could not completely eliminate the CO signal in the DRIFT spectra of Pt/CeO₂-C, which indicates that the adsorbed CO on Pt/CeO₂-C is hardly removed even when the oxygen is available. Obviously, CO is strongly adsorbed on Pt/CeO₂-C, which is considered to be one of the most common factors for reducing the catalytic performance or even deactivation of catalyst [38]. Moreover, the signals of intermediate species of three catalysts, e.g., formate, ethylidyne etc., are still visible in their DRIFTS, as slightly weakened intensity compared with those at the second stage. This indicates these intermediates are unable to be decomposed by oxygen species under the present reaction conditions.

As shown in Fig. 3(a), the Pt/CeO₂-O catalyst has 40 % of C₂H₄ conversion at 30 °C, while almost no C₂H₄ conversion is detected over other two catalysts Pt/CeO₂-C and Pt/CeO₂-R. That means the oxidation of C₂H₄ over Pt/CeO₂-O should undergo through the whole reaction pathway with C₂H₄ adsorption → HCHO → CO → CO₂. The absence of HCHO signal in the DRIFT spectra of Pt/CeO₂-O can be attributed to the

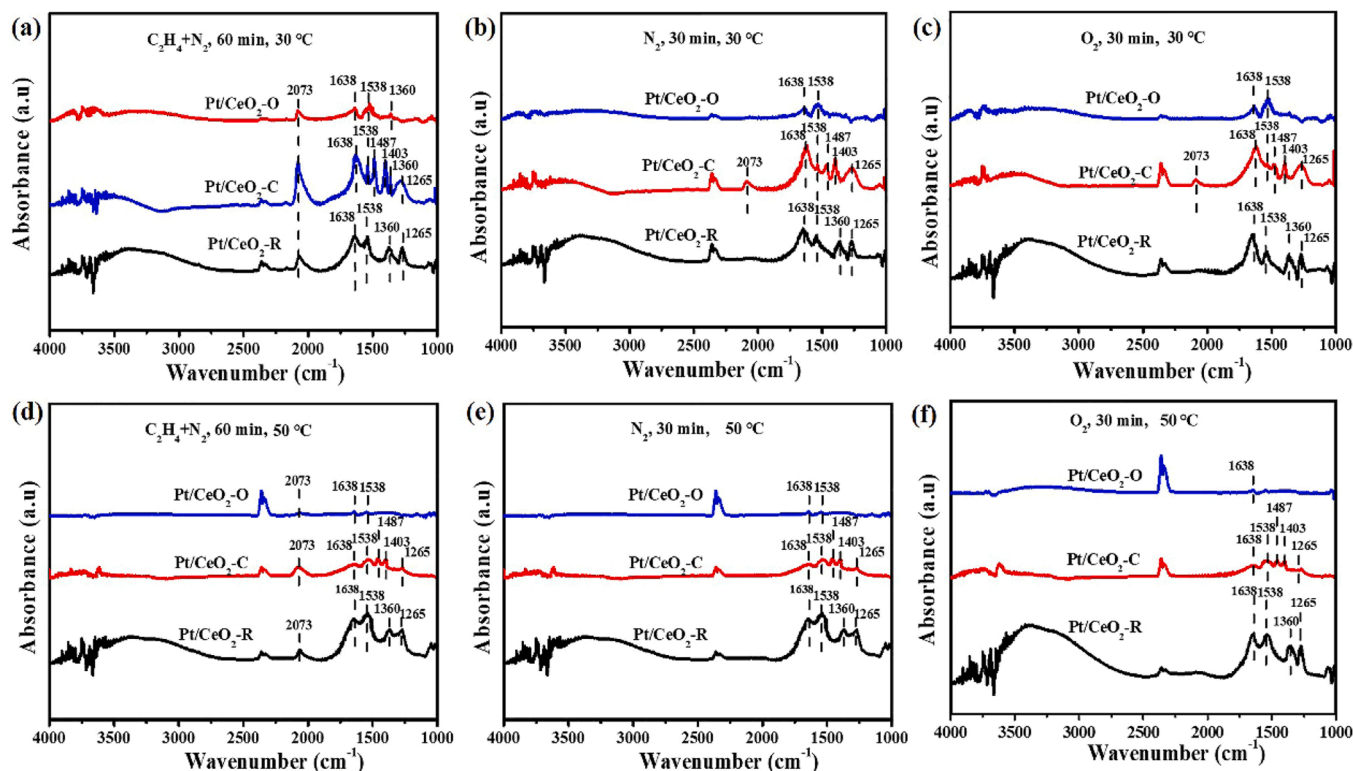


Fig. 7. In-situ C₂H₄-DRIFT spectra of various morphological CeO₂-supported Pt catalysts in the atmospheres of C₂H₄ + N₂, pure N₂ and pure O₂.

rapid reaction from C_2H_4 adsorption to CO. By comparison, the oxidation of linear-adsorbed CO into CO_2 occurs slowly over Pt/CeO₂-O. A small amount of adsorbed HCHO is oxidized into formate, which is diffused onto the CeO₂ surface and consequently is difficult to interact with the Pt nanoparticles of catalysts [4,6,31]. Thus, these formates are hardly decomposed even in the atmosphere of pure oxygen, as demonstrated by our DRIFTS experiments. From the reaction data, it can be seen that the presence of a small amount of formate still permits Pt/CeO₂-O with the low temperature C_2H_4 oxidation performance.

In the C_2H_4 -DRIFT spectra of Pt/CeO₂-C and Pt/CeO₂-R, the oxidation of adsorbed CO is indeed observed. However, CO_2 signal is unable to be detected in the off-gases of Pt/CeO₂-C and Pt/CeO₂-R at the reaction temperature of 30 °C, which is generally attributed to that the CO_2 content of off-gases are below the CO_2 detector or the oxidation of C_2H_4 is shut down. Obviously, the latter reason can account for the no C_2H_4 conversion in catalytic evaluation process of Pt/CeO₂-C and Pt/CeO₂-R. From the DRIFT spectra, it can be observed that large quantities of intermediate species accumulate on Pt/CeO₂-C and Pt/CeO₂-R. The fundamental issue is that the accumulation of intermediate species or their strong adsorptions could cover the active sites to inhibit the adsorption and activation of oxygen or other species, which leads to the decrease in catalytic performance of catalyst and even its deactivation [39,45]. Hence, the accumulation of abundant intermediate species could be responsible for the different reaction pathways of catalysts.

Furthermore, above DRIFTS analyses have mentioned the obviously different types of intermediate species of Pt/CeO₂-C from those of Pt/CeO₂-R. This indicates the discrepant reaction mechanism of C_2H_4 oxidation between Pt/CeO₂-C and Pt/CeO₂-R. As shown in Fig. 8, Pt/CeO₂-C has the more obvious signal of methyl and CO than those of Pt/CeO₂-R. By contrast, the signal intensity of formate in DRIFT spectra of Pt/CeO₂-C is lower, compared with that of Pt/CeO₂-R. Based on above analyses of reaction pathway, it is inferred that the carbon-carbon bond breakage occurs difficultly over Pt/CeO₂-C, consequently for its high intensity of ethylidyne signal. Over Pt/CeO₂-R, the C_2H_4 could undergo through above-mentioned reaction steps of C_2H_4 oxidation over Pt/CeO₂-C. Only the formate is difficult to be decomposed over Pt/CeO₂-R, thus leading to the relatively obvious formate signal.

When the reaction temperature increases to 50 °C, the C_2H_4 conversion could reach up to 100 % over Pt/CeO₂-O, but only 61 % and 34 % for Pt/CeO₂-C and Pt/CeO₂-R, respectively (as seen in Fig. 3). Fig. 7 shows that at the first stage, Pt/CeO₂-O does not show any signal on

intermediate species expect for CO. This illustrates that no accumulation of intermediate species occurs, which could be responsible for the high-efficient C_2H_4 oxidation over Pt/CeO₂-O at 50 °C. Similarly, increasing reaction temperature could significantly weaken the signal intensity of intermediate species over Pt/CeO₂-C and Pt/CeO₂-R although all of them are still present in the DRIFT spectra of catalysts. This might be attributed to the fact that the intermediates cannot be desorbed from the catalyst surface. Therefore, formaldehyde and formic acid are indeed undetectable in GC measurements for final products. This result also in turn demonstrates that the accumulation of intermediate species reduces the low temperature C_2H_4 oxidation performance of Pt/CeO₂-C and Pt/CeO₂-R, which could also be responsible for their higher activation energies of C_2H_4 oxidation than that of Pt/CeO₂-O.

In a summary, the reaction mechanism of low temperature C_2H_4 oxidation over three morphological CeO₂-supported Pt catalysts are proposed, as schematically illustrated in Fig. 8. C_2H_4 preliminarily adsorbs onto the catalyst surface and is promptly reacted with oxygen species to dissociate into adsorbed HCHO over Pt/CeO₂-R and Pt/CeO₂-O. By contrast, the C_2H_4 dissociation over Pt/CeO₂-C is slower so that ethylidyne is formed. Subsequently, the adsorbed HCHO is dehydrogenated into CO, which could occur over three catalysts. When the CO is oxidized into CO_2 , the whole C_2H_4 oxidation process is accomplished. The reaction rate of CO oxidation is relatively faster over Pt/CeO₂-R and Pt/CeO₂-O, while a small amount of CO strongly adsorbed on Pt/CeO₂-C are difficult to be oxidized. Moreover, the adsorbed HCHO is also partially oxidized to generate the formate. In comparison, the formate amount is the most on Pt/CeO₂-R, followed by Pt/CeO₂-C, and the least on Pt/CeO₂-O. Herein, the different rates of some steps of C_2H_4 oxidation can be responsible for the disparate catalytic performance of various morphological Pt/CeO₂ catalysts.

3.5. Structure-performance relationship discussion

According to structural analyses mentioned above, it is confirmed that three Pt/CeO₂ catalysts with different shapes have the dramatically varying structural properties. In this section, the morphological effect of CeO₂ on the low temperature C_2H_4 oxidation performance of corresponding catalysts will be clarified.

Due to the same crystal phases of CeO₂ analyzed by XRD, the influence of crystal phase of CeO₂ on the catalytic performance of catalysts is preliminarily excluded. Moreover, as seen from Table 1, the order in

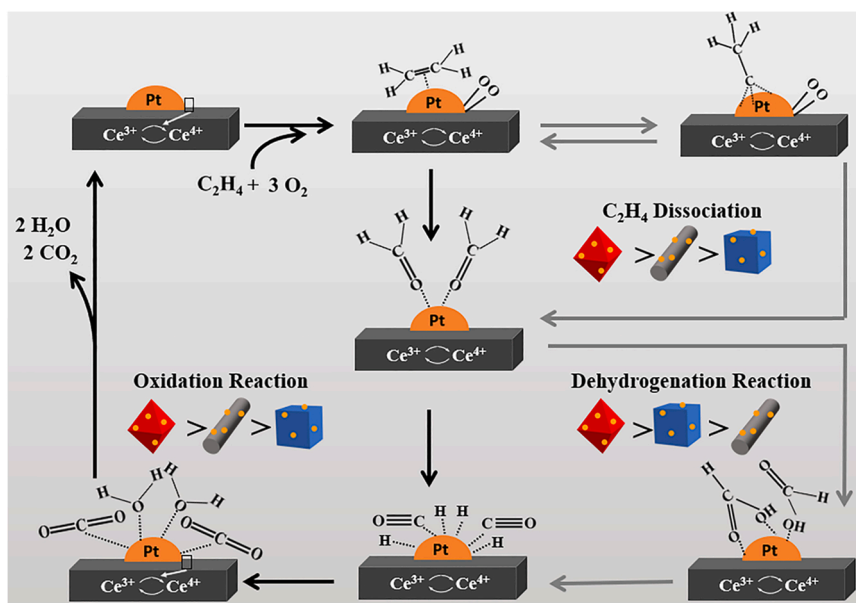


Fig. 8. Scheme for low temperature C_2H_4 oxidation steps over various morphological CeO₂-supported Pt catalysts.

surface area, pore volume and average pore size of three Pt/CeO₂ catalysts does not match with that in their C₂H₄ oxidation performances. Thus, the porous structural properties of Pt/CeO₂ catalysts are also not supposed to be the main factor for influencing their low temperature C₂H₄ oxidation performances.

The following attention is focused on the influence of exposed surfaces of CeO₂. Above HRTEM analyses have demonstrated three catalysts with different exposure crystal planes that Pt/CeO₂-R selectively exposes (110) and (100) crystal planes, Pt/CeO₂-C does (100) crystal planes and Pt/CeO₂-O is enclosed by (111) crystal planes. Essentially, the different exposed surface of CeO₂ gives rises to different coordination of Ce and O atoms, which can further change the states of such two types of superficial atoms and neighboring Pt nanoparticles [25]. Above XPS and Raman analyses have confirmed unequal redox cycle of Ce³⁺/Ce⁴⁺ in three Pt/CeO₂ catalysts due to the presence of different content of Ce³⁺ and Ce⁴⁺ and different amounts of oxygen vacancies. The redox cycle of Ce³⁺/Ce⁴⁺ is considered to influence the activation of surface oxygen species [23]. However, these two structural characteristics of CeO₂ brought by exposed crystal planes do not directly affect the low temperature C₂H₄ oxidation performance of catalysts. The reason is that on three kinds of CeO₂, the oxidation reaction of C₂H₄ molecules starts at least above 145 °C, which is obviously higher than those of corresponding Pt/CeO₂ catalysts (20 ~ 35 °C). Apparently, the low temperature C₂H₄ oxidation performance of Pt/CeO₂ is closely associated with the states of Pt nanoparticles rather than structure of CeO₂. The physicochemical properties of Pt nanoparticles are varied when they are deposited on the different-shaped CeO₂.

The combined analyses of XRD and EDS mapping have demonstrated the excellent Pt dispersion state in three Pt/CeO₂ catalysts. CO-pulse chemisorption and CO-DRIFTS analysis results provide the detailed particle size of Pt nanoparticles that the difference among three Pt/CeO₂ catalysts is less than 0.2 nm. TOF value of C₂H₄ oxidation at 30 °C is calculated to evaluate the influence of particle size of Pt nanoparticles on the low temperature C₂H₄ oxidation performance of Pt/CeO₂ catalysts. The TOF values of various Pt/CeO₂ are $0.7 \times 10^{-2} \text{ s}^{-1}$ for Pt/CeO₂-R, $1.4 \times 10^{-2} \text{ s}^{-1}$ for Pt/CeO₂-C, and $9.0 \times 10^{-2} \text{ s}^{-1}$ for Pt/CeO₂-O, respectively. Obviously, the subtle change in Pt particle size cannot be responsible for the notable difference in TOF values among Pt/CeO₂ catalysts which implies that the different morphological Pt/CeO₂ catalysts possess the dissimilar intrinsic activities of low temperature C₂H₄ oxidation.

Varying from the similar geometric structures, both chemical valence and interaction with CeO₂ of Pt nanoparticles are significantly different in three Pt/CeO₂ catalysts, as demonstrated by XPS and TPR analyses. Pt/CeO₂-O possesses the higher content of metallic Pt species and lower interaction between Pt and CeO₂ than those of Pt/CeO₂-R and Pt/CeO₂-C. As for the influence on oxygen species, TPR, O₂-TPD and XPS analyses have demonstrated that the oxygen species on Pt/CeO₂-O are the most active and abundant. It has been confirmed that the presence of metallic Pt and weak Pt-CeO₂ interaction are beneficial to the activation of oxygen species, which was reported elsewhere [46]. Alternatively, for the influence of reaction pathway on C₂H₄ molecule, C₂H₄-DRIFTS studies have demonstrated that the oxidation of C₂H₄ on three Pt/CeO₂ catalysts proceeds through the same reaction pathway. This indicates three Pt/CeO₂ catalysts possess the same type of active sites even in the presence of the difference in chemical valence and interaction with CeO₂ of Pt nanoparticles [47].

Based on the above discussion, it can be concluded that the activation state of oxygen species on various Pt/CeO₂ catalysts plays a vital role in their low temperature C₂H₄ oxidation performances. More specifically, Pt/CeO₂-O contains the most active and abundant oxygen species, and thus C₂H₄ molecules are prone to dissociation, dehydrogenation and oxidation, consequently the least amounts of intermediate species of C₂H₄ oxidation on Pt/CeO₂-O. In contrast, the relatively poor reactivity and lower amount of oxygen species on Pt/CeO₂-C decrease the rate of reaction steps of dissociation and oxidation, which

consequently is detrimental to the overall efficiency of C₂H₄ oxidation on Pt/CeO₂-C. As for Pt/CeO₂-R, due to the contribution of oxygen species with the worst state, it shows the large accumulation of formate, suggesting the slow rate of dehydrogenation. Note that the order in activation state of oxygen species of three catalysts is identical to that in their *E_a* values. Therefore, it is confirmed that the activation of oxygen species over various morphological CeO₂-supported Pt catalysts can be responsible for their difference in low temperature C₂H₄ oxidation performances.

4. Conclusions

The present work investigated the morphological effect of CeO₂ (rod, cube and octahedron) on the low temperature C₂H₄ oxidation performance of corresponding CeO₂-supported Pt catalysts. The structural properties of CeO₂-supported Pt catalysts were systematically analyzed by various characterizations and their catalytic performances of low-temperature C₂H₄ oxidation were studied. The influencing factors, including porous structure of catalysts, crystal phase of CeO₂ and dispersion state of Pt nanoparticles, were excluded on the low temperature C₂H₄ oxidation performance of various Pt/CeO₂ catalysts. It was confirmed that the type of exposed facets of CeO₂ determined by their shapes could govern the activation state of oxygen species of corresponding CeO₂-supported Pt catalysts. Moreover, the difference in reaction steps of C₂H₄ oxidation among various shaped CeO₂-supported Pt catalysts was clarified, which could be responsible for their discrepant low temperature C₂H₄ oxidation performances. The findings from this work are beneficial to the application of Pt/CeO₂- catalysts in the preservation of F&V.

CRedit authorship contribution statement

Haiying Wei: Conceptualisation, Investigation, Methodology, Validation, Visualisation, Writing – original draft. **Tongtong Wei:** Characterization, **Licheng Li:** Conceptualisation, Writing – review & editing, Funding acquisition. **Tingwei Zhang:** Conceptualization, Writing – review & editing. **Farzad Seidi:** Writing – review & editing. **Yongcan Jin:** Writing – review & editing. **Huining Xiao:** Conceptualisation, Resources, Supervision, Writing – review & editing.

Declaration of Competing Interest

The authors declare that they have no known competing financial interests or personal relationships that could have appeared to influence the work reported in this paper.

Data Availability

Data will be made available on request.

Acknowledgements

The work is supported by the funding from the Jiangsu Co-Innovation Center of Efficient Processing and Utilization of Forest Resources, General Program of National Natural Science Foundation of China (21978134), Jiangsu Province Scientific research and Practice innovation project (KYCX21_0883) and NSERC Canada.

Appendix A. Supporting information

Supplementary data associated with this article can be found in the online version at doi:10.1016/j.apcatb.2022.122242.

References

- [1] N. Keller, M.N. Ducamp, D. Robert, V. Keller, Ethylene removal and fresh product storage: a challenge at the frontiers of chemistry. Toward an approach by photocatalytic oxidation, *Chem. Rev.* 113 (2013) 5029–5070, <https://doi.org/10.1021/cr900398v>.
- [2] H. Wei, F. Seidi, T. Zhang, Y. Jin, H. Xiao, Ethylene scavengers for the preservation of fruits and vegetables: a review, *Food Chem.* 337 (2021), 127750, <https://doi.org/10.1016/j.foodchem.2020.127750>.
- [3] M. Wen, F. Dong, J. Yao, Z. Tang, J. Zhang, Pt nanoparticles confined in the ordered mesoporous CeO₂ as a highly efficient catalyst for the elimination of VOCs, *J. Catal.* 412 (2022) 42–58.
- [4] C.X. Jiang, K.H. Hara, A. Fukuoka, Low-temperature oxidation of ethylene over platinum nanoparticles supported on mesoporous silica (<https://doi.org/http://>), *Angew. Chem. Int. Ed.* 125 (2013) 6265–6268, <https://doi.org/10.1002/anie.201300496>.
- [5] S.S. Satter, J. Hirayama, H. Kobayashi, K. Nakajima, A. Fukuoka, Water-resistant Pt Sites in hydrophobic mesopores effective for low-temperature ethylene oxidation, *ACS Catal.* 10 (2020) 13257–13268, <https://doi.org/10.1021/acscatal.0c02816>.
- [6] S.S. Satter, T. Yokoya, J. Hirayama, K. Nakajima, A. Fukuoka, Oxidation of trace ethylene at 0 °C over platinum nanoparticles supported on silica, *ACS Sustain. Chem. Eng.* 6 (2018) 11480–11486, <https://doi.org/10.1021/acssuschemeng.8b01543>.
- [7] H.G. Ahn, B.M. Choi, D.J. Lee, Complete oxidation of ethylene over supported gold nanoparticle catalysts, *J. Nanosci. Nanotechnol.* 6 (2006) 3599–3603, <https://doi.org/10.1166/jnn.2006.17990>.
- [8] H. Yang, C. Ma, Y. Li, J. Wang, X. Zhang, G. Wang, N. Qiao, Y. Sun, J. Cheng, Z. Hao, Synthesis, characterization and evaluations of the Ag/ZSM-5 for ethylene oxidation at room temperature: Investigating the effect of water and deactivation, *Chem. Eng. J.* 347 (2018) 808–818, <https://doi.org/10.1016/j.cej.2018.04.095>.
- [9] H. Guo, P. Warnicke, M. Griffo, U. Muller, S. Chen, R. Schaeublin, Z. Zhang, M. Lukovic, Hierarchical porous wood cellulose scaffold with atomically dispersed Pt catalysts for low-temperature ethylene decomposition, *ACS Nano* 13 (2019) 14337–14347, <https://doi.org/10.1021/acsnano.9b07801>.
- [10] H. Yang, C. Ma, G. Wang, Y. Sun, J. Cheng, Z. Zhang, X. Zhang, Z. Hao, Fluorine-enhanced Pt/ZSM-5 catalysts for low-temperature oxidation of ethylene, *Catal. Sci. Technol.* 8 (2018) 1988–1996, <https://doi.org/10.1039/c8cy00130h>.
- [11] C. Yang, G. Miao, Y. Pi, Q. Xia, J. Wu, Z. Li, J. Xiao, Abatement of various types of VOCs by adsorption/catalytic oxidation: A review, *Chem. Eng. J.* 370 (2019) 1128–1153, <https://doi.org/10.1016/j.cej.2019.03.232>.
- [12] J.A. Rodriguez, D.C. Grinter, Z. Liu, R.M. Palomino, S.D. Senanayake, Ceria-based model catalysts: fundamental studies on the importance of the metal-ceria interface in CO oxidation, the water-gas shift, CO₂ hydrogenation, and methane and alcohol reforming, *Chem. Soc. Rev.* 46 (2017) 1824–1841, <https://doi.org/10.1039/c6cs00863a>.
- [13] H.A.E. Dole, E.A. Baranova, Ethylene oxidation in an oxygen-deficient environment: why ceria is an active support? *ChemCatChem* 8 (2016) 1977–1986, <https://doi.org/10.1002/cctc.201600142>.
- [14] Q. Wang, K.L. Yeung, M.A. Bañares, Ceria and its related materials for VOC catalytic combustion: a review, *Catal. Today* 356 (2020) 141–154, <https://doi.org/10.1016/j.cattod.2019.05.016>.
- [15] K. Zhou, X. Wang, X. Sun, Q. Peng, Y. Li, Enhanced catalytic activity of ceria nanorods from well-defined reactive crystal planes, *J. Catal.* 229 (2005) 206–212, <https://doi.org/10.1016/j.jcat.2004.11.004>.
- [16] Z. Wu, M. Li, S.H. Overbury, On the structure dependence of CO oxidation over CeO₂ nanocrystals with well-defined surface planes, *J. Catal.* 285 (2012) 61–73, <https://doi.org/10.1016/j.jcat.2011.09.011>.
- [17] L. Torrente-Murciano, A. Gilbank, B. Puertolas, T. Garcia, B. Solsona, D. Chadwick, Shape-dependency activity of nanostructured CeO₂ in the total oxidation of polycyclic aromatic hydrocarbons, *Appl. Catal. B: Environ.* 132–133 (2013) 116–122, <https://doi.org/10.1016/j.apcatb.2012.10.030>.
- [18] M. Li, Z. Wu, S.H. Overbury, Surface structure dependence of selective oxidation of ethanol on faceted CeO₂ nanocrystals, *J. Catal.* 306 (2013) 164–176, <https://doi.org/10.1016/j.jcat.2013.06.019>.
- [19] S. Wang, Y. Wang, F. Wang, Room temperature HCHO oxidation over the Pt/CeO₂ catalysts with different oxygen mobilities by changing ceria shapes, *Appl. Catal. A: Gen.* 630 (2022), 118469.
- [20] H. Tan, J. Wang, S. Yu, K. Zhou, Support morphology-dependent catalytic activity of Pd/CeO₂ for formaldehyde oxidation, *Environ. Sci. Technol.* 49 (2015) 8675–8682, <https://doi.org/10.1021/acs.est.5b01264>.
- [21] Y. Lei, W. Li, Q. Liu, Q. Lin, X. Zheng, Q. Huang, S. Guan, X. Wang, C. Wang, F. Li, Typical crystal face effects of different morphology ceria on the activity of Pd/CeO₂ catalysts for lean methane combustion, *Fuel* 233 (2018) 10–20, <https://doi.org/10.1016/j.fuel.2018.06.035>.
- [22] Q. Zhang, J. Bu, J. Wang, C. Sun, D. Zhao, G. Sheng, X. Xie, M. Sun, L. Yu, Highly efficient hydrogenation of nitrobenzene to aniline over Pt/CeO₂ catalysts: the shape effect of the support and key role of additional Ce³⁺ sites, *ACS Catal.* 10 (2020) 10350–10363, <https://doi.org/10.1021/acscatal.0c02730>.
- [23] R. Schmitt, A. Nanning, O. Kraynis, R. Korobko, A.I. Frenkel, I. Lubomirsky, S. M. Haile, J.L.M. Rupp, A review of defect structure and chemistry in ceria and its solid solutions, *Chem. Soc. Rev.* 49 (2020) 554–592, <https://doi.org/10.1039/c9cs00588a>.
- [24] R. Si, M. Flytzani-Stephanopoulos, Shape and crystal-plane effects of nanoscale ceria on the activity of Au-CeO₂ catalysts for the water–gas shift reaction, *Angew. Chem. Int. Ed.* 120 (2008) 2926–2929, <https://doi.org/10.1002/ange.200705828>.
- [25] R. Peng, X. Sun, S. Li, L. Chen, M. Fu, J. Wu, D. Ye, Shape effect of Pt/CeO₂ catalysts on the catalytic oxidation of toluene, *Chem. Eng. J.* 306 (2016) 1234–1246, <https://doi.org/10.1016/j.cej.2016.08.056>.
- [26] L. Li, L. Li, L. Wang, X. Zhao, Z. Hua, Y. Chen, X. Li, X. Gu, Enhanced catalytic decomposition of formaldehyde in low temperature and dry environment over silicate-decorated titania supported sodium-stabilized platinum catalyst, *Appl. Catal. B: Environ.* 277 (2020), 119216, <https://doi.org/10.1016/j.apcatb.2020.119216>.
- [27] H. Huang, Q. Dai, X. Wang, Morphology effect of Ru/CeO₂ catalysts for the catalytic combustion of chlorobenzene, *Appl. Catal. B: Environ.* 158–159 (2014) 96–105, <https://doi.org/10.1016/j.apcatb.2014.01.062>.
- [28] J. Sun, J. Zhang, H. Fu, H. Wan, Y. Wan, X. Qu, Z. Xu, D. Yin, S. Zheng, Enhanced catalytic hydrogenation reduction of bromate on Pd catalyst supported on CeO₂ modified SBA-15 prepared by strong electrostatic adsorption, *Appl. Catal. B: Environ.* 229 (2018) 32–40, <https://doi.org/10.1016/j.apcatb.2018.02.009>.
- [29] B.E. Hayden, K. Kretschmar, A.M. Bradshaw, R.G. Greenler, An infrared study of the adsorption of CO on a stepped platinum surface (<https://doi.org/>), *Surf. Sci.* 149 (1985) 394–406, [https://doi.org/10.1016/0167-2584\(85\)90819-9](https://doi.org/10.1016/0167-2584(85)90819-9).
- [30] M.J. Kale, P. Christopher, Utilizing quantitative in situ FTIR Spectroscopy To Identify Well-Coordinated Pt Atoms as the Active Site for CO Oxidation on Al₂O₃-Supported Pt Catalysts, *ACS Catal.* 6 (2016) 5599–5609, <https://doi.org/10.1021/acscatal.6b01128>.
- [31] H. Yang, C. Ma, X. Zhang, Y. Li, J. Cheng, Z. Hao, Understanding the active sites of Ag/zeolites and deactivation mechanism of ethylene catalytic oxidation at room temperature, *ACS Catal.* 8 (2018) 1248–1258, <https://doi.org/10.1021/acscatal.7b02410>.
- [32] H. Ha, S. Yoon, K. An, H.Y. Kim, Catalytic CO oxidation over Au nanoparticles supported on CeO₂ nanocrystals: effect of the Au–CeO₂ interface, *ACS Catal.* 8 (2018) 11491–11501, <https://doi.org/10.1021/acscatal.8b03539>.
- [33] W.-W. Wang, W.-Z. Yu, P.-P. Du, H. Xu, Z. Jin, R. Si, C. Ma, S. Shi, C.-J. Jia, C.-H. Yan, Crystal plane effect of ceria on supported copper oxide cluster catalyst for CO oxidation: importance of metal–support interaction, *ACS Catal.* 7 (2017) 1313–1329, <https://doi.org/10.1021/acscatal.6b03234>.
- [34] Parthasarathi, K., R. Bera, Arup Priolkar, P., R. Gayen, Sarode, ionic dispersion of Pt over CeO₂ by the combustion method: structural investigation by XRD, TEM, XPS, and EXAFS (<https://doi.org/>), *Chem. Mater.* 34 (2003) 2049–2060, <https://doi.org/10.1021/cm0204775>.
- [35] R. Peng, S. Li, X. Sun, Q. Ren, L. Chen, M. Fu, J. Wu, D. Ye, Size effect of Pt nanoparticles on the catalytic oxidation of toluene over Pt/CeO₂ catalysts, *Appl. Catal. B: Environ.* 220 (2018) 462–470, <https://doi.org/10.1016/j.apcatb.2017.07.048>.
- [36] D.M. Lei Nie, Haifeng Xiong, Bo Peng, Zhibo Ren, A.D. Xavier Isidro Pereira Hernandez, Meng Wang, L.K. Mark, H. Engelhard, Abhaya K. Datye, Yong Wang, Activation of surface lattice oxygen in single-atom Pt/CeO₂ for low-temperature CO oxidation (<https://doi.org/>), *Science* 358 (2017) 1419–1423, <https://doi.org/10.1126/science.aao2109>.
- [37] E.A. Derevyannikova, T.Y. Kardash, A.I. Stadnichenko, O.A. Stonkus, E. M. Slavinskaya, V.A. Svetlichnyi, A.I. Boronin, Structural insight into strong Pt–CeO₂ interaction: from single Pt atoms to PtOx clusters, *J. Phys. Chem. C* 123 (2018) 1320–1334, <https://doi.org/10.1021/acs.jpcc.8b11009>.
- [38] F.C. Meunier, L. Cardenas, H. Kaper, B. Smid, M. Vorokhta, R. Grosjean, D. Aubert, K. Dembele, T. Lunkenbein, Synergy between metallic and oxidized Pt sites unravelled during room temperature CO oxidation on Pt/Ceria, *Angew. Chem. Int. Ed. Engl.* 60 (2021) 3799–3805, <https://doi.org/10.1002/anie.202013223>.
- [39] M. Kourtelesis, T.S. Moraes, L.V. Mattos, D.K. Niakolas, F.B. Noronha, X. Verykios, The effects of support morphology on the performance of Pt/CeO₂ catalysts for the low temperature steam reforming of ethanol, *Appl. Catal. B: Environ.* 284 (2021), 119757, <https://doi.org/10.1016/j.apcatb.2020.119757>.
- [40] J. Raskó, T. Kecskés, J. Kiss, Formaldehyde formation in the interaction of HCOOH with Pt supported on TiO₂, *J. Catal.* 224 (2004) 261–268, <https://doi.org/10.1016/j.jcat.2004.03.025>.
- [41] A.M. Nadeem, G.I.N. Waterhouse, H. Idriss, The reactions of ethanol on TiO₂ and Au/TiO₂ anatase catalysts, *Catal. Today* 182 (2012) 16–24, <https://doi.org/10.1016/j.cattod.2011.08.051>.
- [42] R.M. Rioux, J.D. Hoefelmeyer, M. Grass, H. Song, K. Niesz, P. Yang, G.A. Somorjai, Adsorption and Co-adsorption of ethylene and carbon monoxide on silica-supported monodisperse Pt nanoparticles: volumetric adsorption and infrared spectroscopy studies, *Langmuir* 24 (2008) 198–207, <https://doi.org/10.1021/la702685a>.
- [43] T. Kecskés, J. Raskó, J. Kiss, FTIR and mass spectrometric studies on the interaction of formaldehyde with TiO₂ supported Pt and Au catalysts, *Appl. Catal. A: Gen.* 273 (2004) 55–62, <https://doi.org/10.1016/j.apcata.2004.06.012>.
- [44] L. Wang, H. Yue, Z. Hua, H. Wang, X. Li, L. Li, Highly active Pt/NaxTiO₂ catalyst for low temperature formaldehyde decomposition (<https://doi.org/>), *Appl. Catal. B: Environ.* 219 (2017) 301–313, <https://doi.org/10.1016/j.apcatb.2017.07.073>.
- [45] Q. Zhang, S. Mo, J. Li, Y. Sun, M. Zhang, P. Chen, M. Fu, J. Wu, L. Chen, D. Ye, In situ DRIFT spectroscopy insights into the reaction mechanism of CO and toluene co-oxidation over Pt-based catalysts, *Catal. Sci. Technol.* 9 (2019) 4538–4551, <https://doi.org/10.1039/c9cy00751b>.
- [46] T. Tong, X. Liu, Y. Guo, M. Norouzi Banis, Y. Hu, Y. Wang, The critical role of CeO₂ crystal-plane in controlling Pt chemical states on the hydrogenolysis of furfuryl alcohol to 1,2-pentanediol, *J. Catal.* 365 (2018) 420–428, <https://doi.org/10.1016/j.jcat.2018.07.023>.
- [47] S. Yoon, H. Ha, J. Kim, E. Nam, M. Yoo, B. Jeong, H.Y. Kim, K. An, Influence of the Pt size and CeO₂ morphology at the Pt–CeO₂ interface in CO oxidation, *J. Mater. Chem. A* 9 (2021) 26381–26390, <https://doi.org/10.1039/d1ta06850d>.